Characteristics of Modified Single-Defect Two-Dimensional Photonic Crystal Lasers

Hong-Gyu Park, Jeong-Ki Hwang, Joon Huh, Han-Youl Ryu, Se-Heon Kim, Jeong-Soo Kim, and Yong-Hee Lee

***Abstract*—The resonant modes found in a modified single-defect two-dimensional photonic crystal slab structure are theoretically and experimentally studied. There exist several modes in the band gap: doubly degenerate (dipole and quadrupole modes) and nondegenerate (hexapole and monopole modes). Among them, the monopole mode specifically attracts our interest because of its nondegeneracy, good coupling with the gain medium, and existence of the intensity minimum at the center of the cavity, which would open up the chance for the electrically driven single-defect laser. The nondegenerate hexapole mode, a special type of whispering gallery mode, has a very high quality factor. We have fabricated two types of modified single-defect lasers, i.e., air-based free-standing and SiO_2-based epoxy-bonded structures. Rich lasing actions in both structures are experimentally observed under optically pulsed pumping conditions at room temperature. In the free-standing slab structure, photons are strongly confined in vertical direction, and the lasing operations of all resonant modes with low thresholds are obtained. Especially, the nondegenerate monopole-mode laser is confirmed to have a large spontaneous emission factor of $>$0.06, estimated by analyzing rate equations. In the SiO_2-based slab structure, thermal properties are improved at the expense of vertical losses.**

***Index Terms*—FDTD, InGaAsP–InP, microcavity, photonic band gap, semiconductor laser, spontaneous emission factor.**

I. Introduction

Owing to the advancement of the semiconductor nanofabrication techniques, it is now possible to make a wavelength-sized microcavity. The microcavity containing an active material can be an efficient low-threshold laser when the low cavity loss is assumed [1], [2]. As a potential candidate of the thresholdless laser, the photonic crystal single-defect laser is often considered [3]–[5]. This photonic crystal microcavity with a small modal volume of $\sim(\lambda/2n)^3$ and high-quality factor (Q factor) is expected to actualize the ultimate goal.

Photonic crystal defect lasers have been mainly fabricated in the slab type of structure due to its simplicity in fabrication and analysis [6]–[8]. In such a slab, a photon is three-dimensionally (3-D) confined by following two effects: two-dimensional (2-D) photonic crystal defined on the slab (lateral direction) and total internal reflection by slab waveguide (vertical direction). Various kinds of photonic crystal lasers have been reported recently [5], [9]–[12]. As one of those, we introduce a following scheme: it is known that a conventional 2-D single-defect photonic crystal cavity supports only doubly degenerate dipole modes in the photonic band gap (PBG). One can lift this degeneracy by introducing an asymmetry into the structure [13]. However, the intentional asymmetry results in the increase of the cavity loss, i.e., the decrease of the Q factor [7]. As one possibility toward the ultimate laser, we suggest using other resonant modes that are nondegenerate. By suitable modification of the lateral periodic patterns around the defect, other modes initially buried in the air band can be made to appear into the band gap. Among these modes, we recently proposed the nondegenerate monopole mode and reported its lasing action [5]. In this paper, we will discuss characteristics of the several resonant modes including the monopole mode.

Free-standing slab structures are widely employed because they are relatively easy to fabricate. However, this type of structure has poor mechanical stability and thermal conductivity. If a low-index material, e.g., SiO_2 or Si_3N_4, is substituted for the air as a bottom cladding, better thermal conduction can be obtained. Actually, this was experimentally shown [10], and continuous-wave (CW) PBG lasing operation was also successfully realized from a cavity having many defects at room temperature [11]. However, in a single-defect cavity of this structure, the lasing action has not been observed due to the low-Q factor. On the other hand, our modified single-defect cavity can support several high-Q modes that can be made into lasers.

We begin this paper by introducing some resonant modes shown in the modified single-defect cavity in Section II. From the field profile of each mode, their mode properties are discussed. In Section III, the fabrication processes of two structures, free-standing and epoxy-bonded slab structures, are described. Section IV is devoted to discuss properties of the modified single-defect structure in the free-standing slab. The Q factors of the resonant modes are obtained by the 3-D finite-difference time-domain (FDTD) method [14], and their experimental results, spectra, mode shapes, collected power at lasing wavelength versus the peak pump power (L–L) curves, and polarizations, are analyzed under optically pulsed pumping conditions. Specifically, by rate equation analysis, the spontaneous emission factor (β factor) of the monopole mode is estimated. In Section V, characteristics of the PBG structures with SiO_2-bottom cladding layers are analyzed. Like the previous section, the Q factors of the modes are calculated under several different conditions, and optical pumping is performed at room temperature. Finally, we conclude these subjects in Section VI with hope for the thresholdless laser.

Manuscript received March 18, 2002; revised July 8, 2002. This work was supported by the National Research Laboratory Project of Korea and the NICOP program of the Office of Naval Research.

H.-G. Park, J. Huh, H.-Y. Ryu, S.-H. Kim, J.-S. Kim, and Y.-H. Lee are with the Department of Physics, Korea Advanced Institute of Science and Technology, Taejon, Korea.

J.-K. Hwang is with the Networking Solution Division, Agilent Technologies, San Jose, CA 95131 USA.

Publisher Item Identifier 10.1109/JQE.2002.802951.

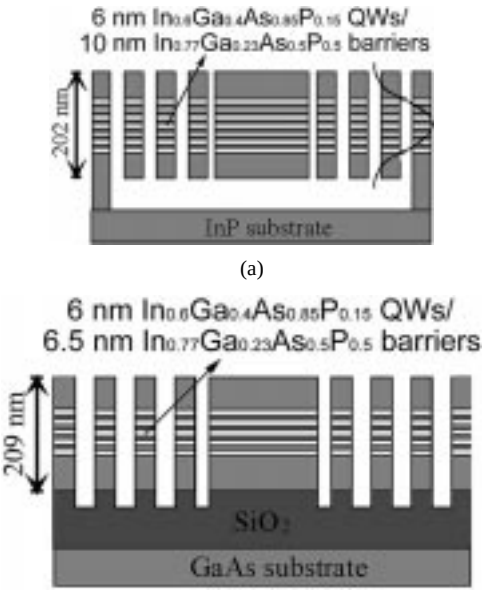

Fig. 1. Schematic diagrams of (a) the free-standing slab structure and (b) the oxide-based slab structure. (a) The thickness of the slab waveguide is 202 nm and seven 6-nm $In_{0.6}Ga_{0.4}As_{0.85}P_{0.15}$ QWs are employed. Only the lowest TE mode is allowed in this structure due to the thin slab thickness. (b) Five 6-nm $In_{0.6}Ga_{0.4}As_{0.85}P_{0.15}$ QWs are also contained in the active slab. Thick SiO_2 layer, over 500 nm, and GaAs substrate are bonded by epoxy.

II. Tuning of the Structure

A. Free-Standing Slab Structure

In our laser structure, seven 6-nm strain-compensated indium gallium arsenic phosphide (InGaAsP) quantum wells (QWs) are used as an active material whose photoluminescence (PL) peak is located at 1.55 μm [Fig. 1(a)]. An InGaAsP–InP material system is widely employed for photonic crystal structures that have many air holes, because of its relatively slow surface recombination velocity [3], [15]. A low-loss cavity is formed on a free-standing slab by defining periodic triangular lattice of air holes. Only the lowest transverse-electric (TE) mode is allowed in the thin slab waveguide including the active material, whose thickness is $\sim\lambda/2$ (202 nm). Also, strong coupling between cavity modes and the gain region is obtained by deep air holes drilled down to the QWs.

As mentioned earlier, the cavity needs to be modified in order to find other usable modes. If one reduces and pushes away the nearest neighbor holes as shown in Fig. 2(a), the effective cavity size is slightly enlarged, and accordingly, some modes initially in the air band are pulled down into the band gap. Fig. 3 shows the calculated frequency dependence of each mode as a function of the radius of the nearest neighbor holes. As the radius decreases, the dipole modes moves toward the dielectric band and other modes begin to show up in the band gap. This calculation is performed by the 3-D FDTD method when the lattice constant a is 0.57 μm and the radius of the regular holes r is 0.35 a. Slab thickness is fixed to be 0.4 a. Fig. 4 shows the calculated intensity field profiles of the modes. According to their mode shapes, they are hence named [16] *doubly degenerate*, dipole and quadrupole modes [Fig. 4(a) and (b)], or *initially nondegenerate*, hexapole and monopole modes [Fig. 4(c) and (d)]. The nondegerate modes attract our interest due to the expectation

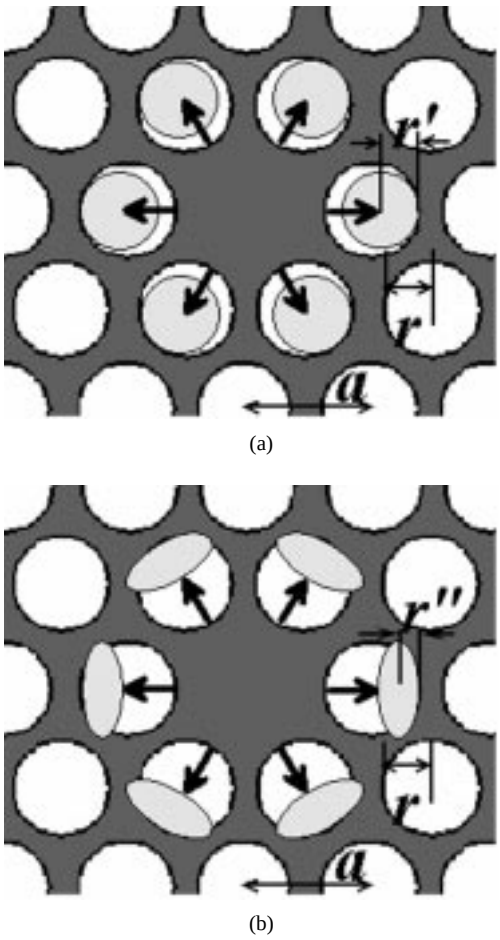

Fig. 2. (a) Modified single-defect structure. By reducing and pushing away the nearest neighbor holes around the defect, it is possible to find other modes including the monopole mode in the band gap. (b) As another tuning of the structure, elliptical-shaped nearest neighbor holes are tried. Only the radius of the minor axis (r'') is varied and other parameters are the same as (a).

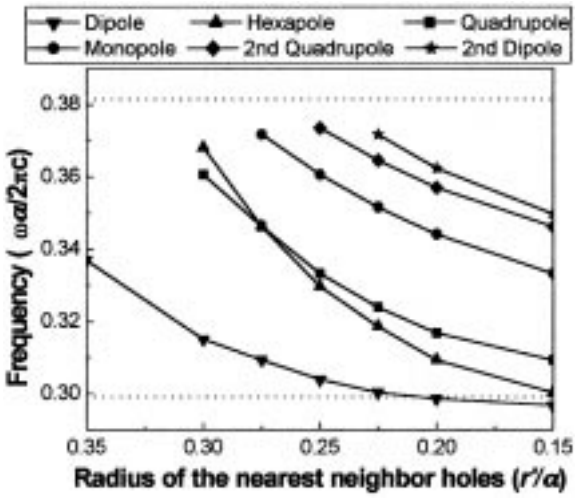

Fig. 3. Frequencies of the resonant modes in the free-standing slab are plotted as a function of radius of the nearest neighbor holes r'. In this calculation performed by 3-D FDTD method, the modified singe defect structure of Fig. 2(a) is tried. The radius of the regular holes and slab thickness are fixed to be 0.35 a and 0.4 a, respectively. Two dotted lines represent band edge frequencies. Even in the other structures with the elliptical-shaped nearest neighbor holes [Fig. 2(b)] or oxide bottom cladding, a similar frequency tendency is shown.

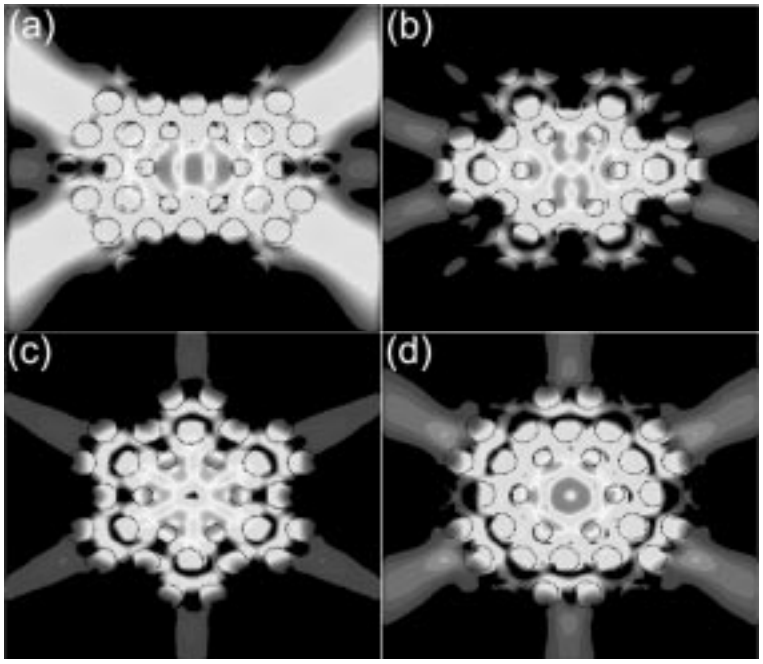

Fig. 4. Top views of the intensity profiles in (a) dipole, (b) quadrupole, (c) hexapole, and (d) monopole modes. These are calculated by 3-D FDTD method under the same conditions as Fig. 3. The radius of the nearest neighbor holes is 0.25 a. While the dipole and quadrupole modes are doubly degenerate, the hexapole and monopole modes are nondegenerate.

of a large β factor. Specifically, the monopole mode has good overlap with the defect region where the gain is generated, contrary to the hexapole mode. Thus, the monopole mode is thought to be more advantageous to lasing action than the other modes. The monopole mode also has a better chance to operate as a single mode. The hexapole and quadrupole modes are close to each other (Fig. 3). On the other hand, adjacent modes near the monopole mode are located far enough from it. The quadrupole mode is $>$110-nm away from the monopole mode and above modes are $>$55-nm apart, when the center wavelength is chosen to be 1.55 μm. These distances are large enough to isolate the monopole mode solely in the gain spectrum of $\sim$100-nm width.

For further optimization, we try the elliptical-shaped nearest neighbor holes around the defect like Fig. 2(b); only the minor axis of the nearest neighbor holes (r'') is varied. All resonant modes of Fig. 4 are obtained from this structure, and the similar but slightly increased frequencies are shown as compared with the case of the previous circular-shaped structure (Fig. 3). Noticeably, the spectral distances between the monopole and its neighboring modes are relatively larger such that chance for the single modeness increases. When the central wavelength of 1.55 μm is also assumed, the monopole mode is $>$97 nm, far from the other nearest neighbor resonant modes, as the radius of the minor axis is smaller than 0.2 a.

B. Oxide-Cladding Slab Structure

Here, we try the modified single-defect slab structure whose bottom cladding is a thick SiO_2 layer instead of the air. Fig. 1(b) shows the schematic diagram of this structure. The dielectric bottom cladding with the low refractive index $\sim$1.5 at 1.5-μ m wavelength results in the increased total effective refractive index and decreases the normalized frequencies of the resonant modes a/λ as compared with the case of the free-standing slab structure [16]. Accordingly, the lattice constant *a* should be smaller than that of the previous structure. When the circular-shaped nearest neighbor holes of Fig. 2(a) are tried, nearly the same frequency dependence as Fig. 3 is also calculated. In this time, the frequencies of all modes are just slightly reduced.

III. Fabrication

A. Free-Standing Slab Structure

The modified single-defect PBG slab structure of Fig. 1(a) is fabricated as follows: 1000-Å-thick 2% poly(methylmethachrolyne) (PMMA) is coated on the top surface of the wafer and triangular lattice PBG patterns are written by electron-beam lithography as in Fig. 2(a). Only circular-shaped nearest neighbor holes are tried. Samples of various parameters are fabricated, based on the calculation results of Fig. 3, to locate each mode near the center of the band gap. The lattice constant (a), radius of the regular holes (r), and radius of the nearest neighbor holes (r') are varied around 0.57 μm, 0.35 a, and 0.225 a, respectively. After developing process, dry etching process is continued. Ion milling using Ar gas hardens the PMMA, and Ar/Cl_2 chemically assisted ion beam etching (CAIBE) is performed in order to drill down to bottom of the slab. PMMA is removed by using O_2 plasma since the chemical property of PMMA is changed during the dry-etching process. Finally, diluted HCl solution separates the slab waveguide containing QWs from the InP substrate, and a free-standing 2-D PBG slab structure is then completed. Fig. 5 shows the SEM picture of the top view of the fabricated PBG structure. In this picture, we note that the distances between the nearest neighbor holes and the defect center are slightly different from our design of the Fig. 2(a). Actually, fabricated positions of the nearest neighbor holes are $\sim$0.93 times closer than the desired

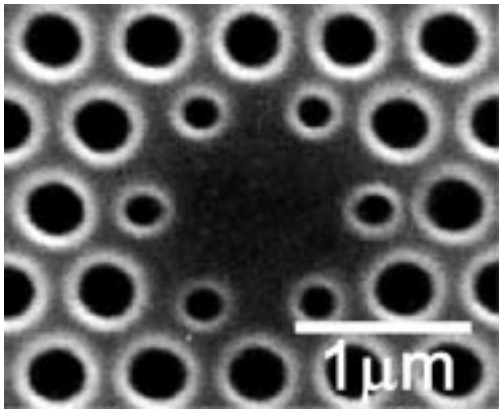

Fig. 5. SEM picture of a fabricated free-standing slab structure. Lattice constant (a) and hole sizes (r, r') of this sample are as follows: $a \sim 0.57\,\mu$m, $r \sim 0.33\,a$, $r' \sim 0.23\,a$. These parameters are estimated by averaging several holes around the defect. Actually fabricated positions of the nearest neighbor holes are $\sim$0.93 times closer than the desired ones.

ones, on the average of some samples. This change affects the frequencies and the Q factors of the resonant modes—all frequencies become increased and Q factors are decreased.

B. Oxide-Cladding Slab Structure

For this structure, additional steps of deliberate process are required. First, a thick dielectric layer, SiO_2, is deposited on the wafer containing InGaAsP QWs, whose thickness is over 500 nm. Then, this dielectric layer is bonded with bare GaAs wafer by epoxy [17]–[19]. The InP substrate of the active wafer is removed by diluted HCl solution, and triangular periodic air holes of Fig. 2(a) are defined using the same method as in Section II-A. As mentioned in Section II, due to the increased effective refractive index, lattice constant a is designed to be a smaller value. The lattice parameters are varied around the following values: a =0.5 μm, radius of the regular holes of $r = 0.4\,a$, and radius of the nearest neighbor holes of $r' = 0.3\,a$. By deep dry etching of CAIBE, air holes are drilled down to the SiO_2 layer. [Fig. 1(b)]. After O_2 ashering, this fabrication process is finished.

IV. Characteristics of Resonant Modes in Free-Standing Slab Structures

A. Calculation of Q Factors

The Q factor of each resonant mode is calculated by using the 3-D FDTD method. If a resonance is excited inside the cavity by a short Gaussian pulse, the energy of this mode gradually decreases by the cavity losses. The total Q factor can be calculated for each mode by analyzing this respective energy decay time. The calculation domain is surrounded by a perfectly matched layer (PML), and reflected electromagnetic waves at the boundary never come back inside the domain [14]. In the slab structure, the total Q factor can be decomposed into in-plane and vertical Qs. The in-plane Q factor increases monotonically with the calculation domain size; on the other hand, the vertical Q factor does not. Thus, the total Q factor is limited by the vertical component [7]. Here, our FDTD calculation domain contains nine air holes along the Γ–K direction, and the distance between the slab and PML boundary is $\sim 5a/2$ [Fig. 6(a)]. The in-plane Q factor is obtained from the absorption at the PML boundary that lies between $\lambda/2$ above the surface of the slab and $\lambda/2$ below it. The vertical Q factor is calculated from the absorption of the rest boundary [7]. The effect of domain size will be discussed later.

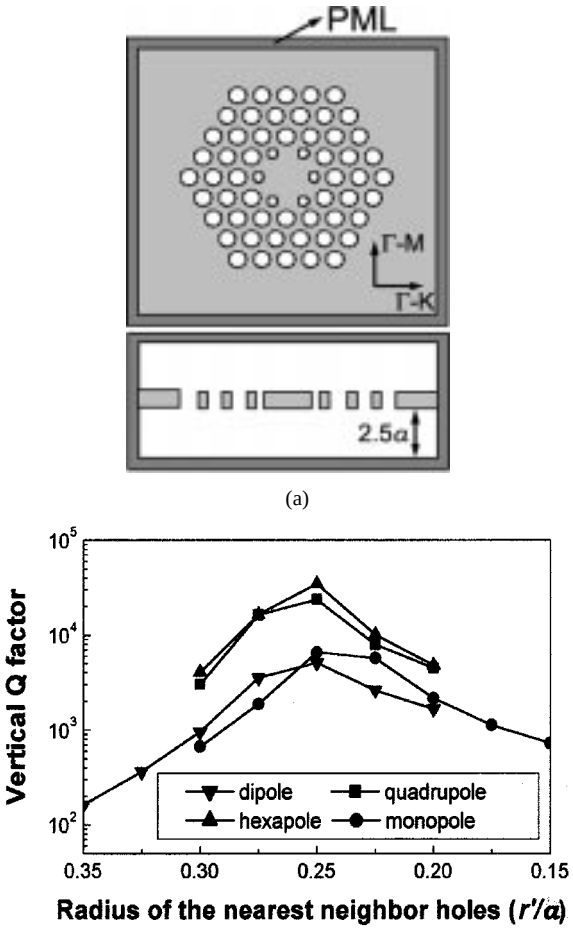

Fig. 6. (a) Top and side views of the domain actually used in our 3-D FDTD calculation. Each is surrounded by a PML boundary, and nine air holes along the Γ–K direction are included in the domain. In the side view, the size of the air region outside the slab is large enough ($\sim 5a/2$) to contain all vertical distributions of modes. (b) Calculated vertical Q factors of four resonant modes in the free-standing slab structure as a function of the radius of the nearest neighbor holes. The radius of the regular holes and the slab thickness are fixed to be 0.35 a and 0.4 a, respectively.

First, we try to calculate Q factors of four resonant modes observed in the free-standing slab structure. In the case of Fig. 2(a) (circular-shaped nearest neighbor holes), their vertical Q factors are evaluated as a function of the radius of the nearest neighbor holes r' when regular hole size r s 0.35 a and slab thickness t, is 0.4 a [Fig. 6(b)]. For all modes, maximum Q values are emerged at $r' = 0.25\ a$. Note that the hexapole mode has the largest maximum vertical Q factor: $\sim$34 000. This very high-Q factor is caused by a similar mode pattern to a whispering-gallery mode (WGM). As shown in Fig. 4(c), the hexapole mode can be considered a first-order WGM whose azimuthal mode number is three. However, while the general WGM is doubly degenerate, the hexapole mode is nondegenerate [20] because degeneracy along azimuthal angle in photonic crystals becomes

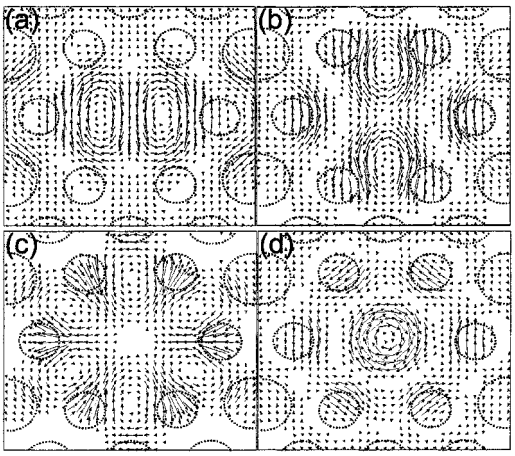

Fig. 7. Electric field directions of (a) dipole, (b) quadrupole, (c) hexapole, and (d) monopole modes. The dipole and quadrupole modes have some oscillating directions; on the other hand, the monopole and hexapole modes have no preferred directions. Calculation parameters are the same as Fig. 3.

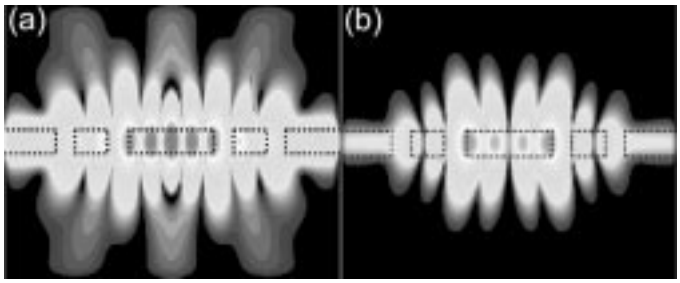

Fig. 8. Side views of the intensity profiles in (a) dipole and (b) hexapole modes. These are calculated by 3-D FDTD method under the same conditions as Fig. 3. Under these conditions, vertical Q factors of each mode have maximum values.

broken by their periodic dielectric arrays. This type of the special WGM is also observed in a square lattice structure [12]. These modes with both high-Q factors and small modal volumes can offer great opportunities to study cavity quantum electrodynamics (QED). Next, the dipole modes show the lowest Q factor, $\sim$5000, among the four modes. This is simply understood by analyzing their electric field directions, as shown in Fig. 7(a). Because of the unbalance in the amplitudes of the positive and negative antinodes, the radiation along normal direction is not effectively suppressed and this vertical loss reduces their vertical Q factors. On the other hand, the electric-field directions of the hexapole mode [Fig. 7(c)] can be paired with opposite phases. All of these pairs generate destructive interferences in the vertical direction and vertical Q factor increases. In the cases of the quadrupole and monopole modes, similar situations arise [Fig. 7(b) and (d)], and relatively high-Q factors are obtained. In Fig. 8(a) and (b), it is visually shown that the confinement of the dipole mode is weaker than that of the hexapole mode.

The monopole mode, attractive for its intrinsic nondegeneracy and good coupling with the defect region, has vertical Q factor of $\sim$6500. Contrary to our expectation, this value is smaller than that of the hexapole mode, although the modes are both hexagonally symmetric. In order to increase this Q factor,

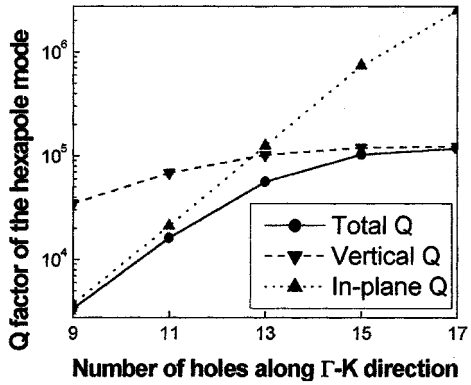

Fig. 9. Total, vertical, and in-plane Q factors of the hexapole mode are evaluated as a function of the calculation domain size. In this calculation, following parameters are used: $r = 0.35\,a$, $r' = 0.25\,a$, and $t = 0.4\,a$. As the number of the hole layers increases, the total Q factor approaches the vertical value.

we try the defect structure of Fig. 2(b) (elliptical-shaped nearest neighbor holes). When the radius of the minor axis in the ellipse (r'') is 0.225 a, the vertical Q factor of the monopole mode is increased up to $\sim$10 000. This structure is more advantageous through its single modeness of the monopole mode (Section II) and its Q factor.

In general, theoretical Q factors depend on the size of the calculation domain. In order to check this effect, the number of holes is varied from 9 to 17 along Γ–K direction in the domain, while all the parameters are fixed to be the same as the previous calculations. In Fig. 9, the vertical and in-plane Q factors of the hexapole mode are calculated as a function of the number of the hole layers. While the in-plane value increases rapidly with the domain size, the vertical value increases only slightly. Also, it is clearly shown in this figure that the total Q factor approaches the vertical value asymptotically as the number of the hole layers increases. All the other modes also show a similar tendency with the domain size.

The slab thickness t is another important parameter to decide the property of the mode. Until now, we have considered thin slabs with thickness of 0.4 a for single-mode vertical confinement. In general, as t increases, the Q factor, as well as the volume of the mode, together increase. Thus, to satisfy the single-mode condition and the high-Q factor simultaneously, t should be well optimized. Fig. 10(a) and (b) show vertical and in-plane Q factors, respectively, of four modes as a function of t. While their vertical Q factors drastically increase with the slab thickness, the in-plane values do not increase continuously; they start to decrease after passing a certain thickness, $\sim$0.5 a. This drop of the in-plane Q factors is attributed to the arrival of the second vertical mode pulled down inside the gap. In other words, some photons tend to couple with this new mode. Therefore, the slab thickness of $\sim$0.5 a is suitable for both the high-Q factor and single-mode condition.

The spontaneous emission enhancement in a microcavity is one of the consequences of the cavity QED. The spontaneous emission rate of a resonant mode in a low-loss cavity is enhanced by amount known as a Purcell factor under the condition that the emission linewidth of an active material is narrower than

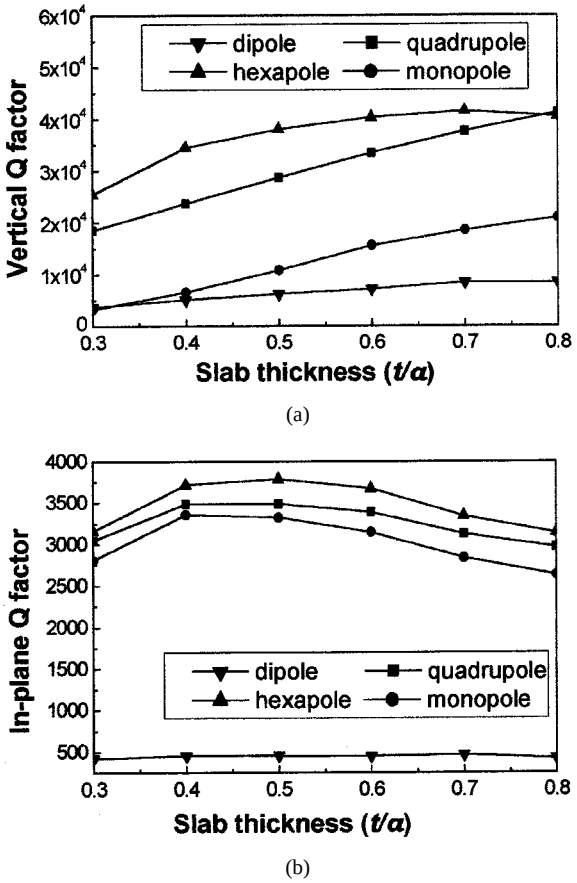

Fig. 10. (a) Vertical and (b) in-plane Q factors of four resonant modes are calculated as a function of the slab thickness t, when $r = 0.35\ a$ and $r' = 0.25\ a$.

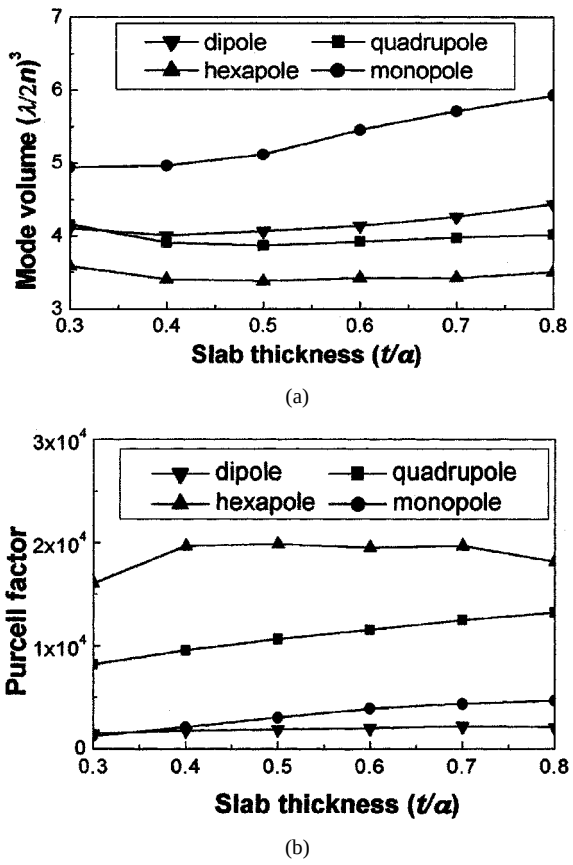

Fig. 11. (a) Mode volumes of the resonant modes are calculated as a function of the slab thickness t. n is refractive index of the slab: 3.4. (b) By using the calculated Q factors and mode volumes, the Purcell factor of each mode is obtained. The hexapole with the smallest mode volume and the highest-Q factor shows the largest Purcell factor. All calculations are performed under $r = 0.35\,a$ and $r' = 0.25\ a$.

the cavity resonance linewidth [4]. The Purcell factor F_p is expressed as follows [6]:

$$F_p = \frac{Q}{4\pi V}\left(\frac{c}{n_{\text{eff}}\nu}\right)^3$$

where Q, V, n_{eff}, and ν are a Q factor, modal volume, effective refractive index, and resonant frequency, respectively. Using this value, one can compare different kinds of microcavities for the enhancement of spontaneous emission. In order to evaluate Purcell factors of the above four resonant modes, their modal volumes are first calculated in Fig. 11(a) as a function of the slab thickness when $r = 0.35\ a$ and $r' = 0.25\ a$. The monopole mode has the largest modal volume $\sim 5(\lambda/2n)^3$ and the hexapole mode has the smallest one of $\sim 3.5(\lambda/2n)^3$, where n is the refractive index of the slab, and is equal to 3.4. These values are about 1.4∼2.0 times larger than the modal volume of a dipole mode in a normal single-defect cavity [8] due to the modified cavity structure. With already calculated Q factors, Purcell factors are obtained in Fig. 11(b). The hexapole mode with the smallest modal volume and the highest-Q factor has the largest F_p of ∼20 000 which is large enough to observe strong QED effects. However, its experimental demonstration, measurement of the spontaneous emission modification, is nontrivial due to the dephasing effect and the low output power from the cavity.

It is interesting to imagine the possibility of electrical pumping in this structure by using the monopole mode, whose mode shape is very unique. The monopole mode has the intensity minimum at the center with hexagonal symmetry, as shown in Fig. 4(d). It is expected that introduction of a small post at this node (inset of Fig. 12) hardly affects the characteristics of the monopole mode while current injection is possible. We calculate the vertical Q factor of the monopole mode with a post in Fig. 12. As expected, this value is not noticeably degraded. Also, other modes with maximum intensity at the center will strongly feel the existence of this post. Therefore, the monopole mode can be advantageous for electrical pumping.

Finally, we calculate the Q factor of the monopole mode with the parameters taken from actually fabricated samples (Section III). In Fig. 13, vertical, in-plane, and total Q factors are evaluated as a function of the radius of the nearest neighbor holes. A high vertical Q factor, over 3700, is obtained at $r' = 0.225\ a$, and this value is slightly different from that of Fig. 6.

B. Experiments

The fabricated free-standing slab structures are optically pumped using a 980-nm laser diode at room temperature. Since this slab has poor thermal conductivity, very short pulses are used. During pumping with ∼10-ns pulses of ∼1% duty cycle,

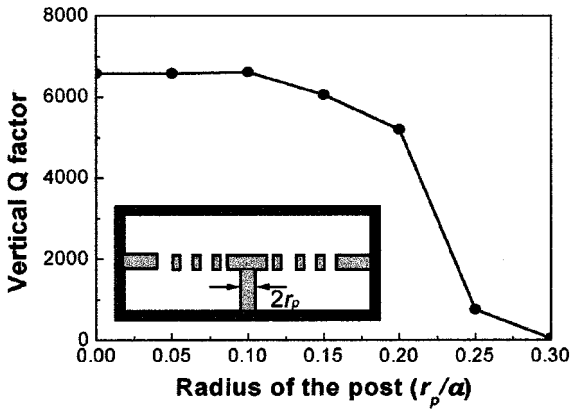

Fig. 12. Vertical Q factor of the monopole mode is calculated as a function of the radius of the post r_p, when there exists a post at the node of the center (inset). The following values are employed: $r = 0.35\ a$, $r' = 0.25\ a$, and $t = 0.4\ a$. The Q factor does not seriously decrease up to $r_p \sim 0.2\ a$.

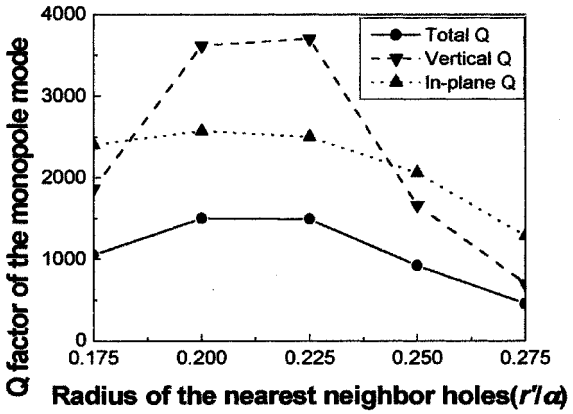

Fig. 13. Calculated Q factors of the monopole mode. Both the regular hole size (r) and slab thickness (t) are fixed to be 0.35 a; the calculation domain contains nine air holes along Γ–K direction. In the same structure as the fabricated sample, only the radius of the nearest neighbor holes (r') is varied. High vertical Q factor, over 3700, is obtained at $r' = 0.225\ a$.

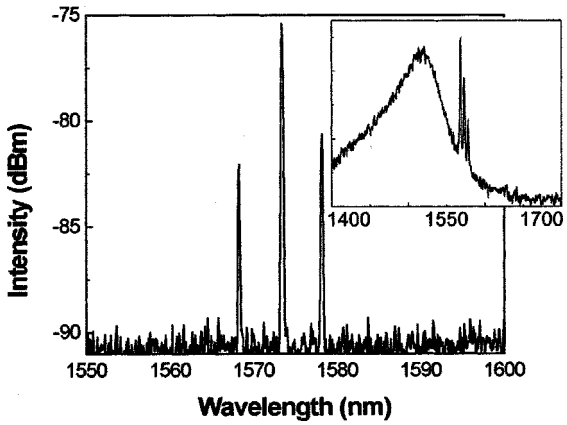

(a)

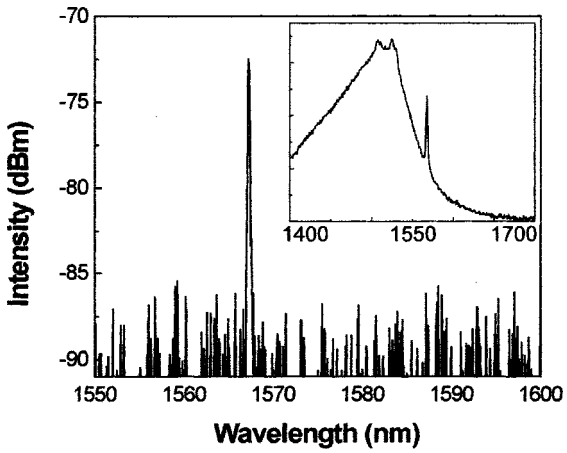

(b)

Fig. 14. Typical above-threshold spectra of (a) the hexapole and two-split quadrupole modes and (b) the monopole mode. Each inset indicates the spectrum below threshold. The monopole-mode laser is measured at 1567-nm wavelength.

an objective lens whose numerical aperture (N.A.) is 0.85 focuses the pump beam to a spot more than 4 μm in diameter and collects output light coming out from the top of the slab. This pump beam size is large enough to make broad mirror region around the defect transparent. Then rich lasing actions are obtained in the samples with various lattice parameters. Fig. 14(a) and (b) show typically observed two types of lasing spectra above threshold. The inset of each figure describes below-threshold spectrum. In Fig. 14(a), three multimode lasing actions indicate the hexapole and two-split quadrupole modes, respectively. They can be well compared with the theoretically obtained frequencies. Because of the slight asymmetry introduced during the fabrication processes, doubly degenerate quadrupole modes are split into two frequencies. The resonance frequencies of hexapole and quadrupole modes are almost the same, and these modes are simultaneously observed. On the other hand, Fig. 14(b), which indicates the monopole-mode spectrum, shows a single-mode lasing action above threshold. Here, the dipole, hexapole, and quadrupole modes do not appear even in the broad PL spectrum [inset of Fig. 14(b)] due to the distant gap from the monopole mode as seen in Fig. 3. Higher resonant modes in the spectrum exist only below threshold, such as the second quadrupole modes, which are located right above the monopole mode in Fig. 3. However, these higher modes have relatively low-Q factors, whose vertical value is ∼1500, as compared with that of the monopole mode, ∼3700, when the FDTD calculation is performed with the experimentally fabricated lattice parameters (Fig. 13). Also, in addition to their poor coupling with the gain region, it seems to be very difficult for these higher modes to overcome cavity losses. In this sense, the nondegenerate monopole-mode laser can operate as a single mode and still be expected to have a large β factor. Actually, the β factor of the monopole mode can be confirmed in the *L–L* curve of Fig. 15, which is a measurement of the collected power at lasing wavelength as a function of the peak pump power. Note that the low-threshold pump power of less than 0.55 mW and the gradual turn-on near the threshold (inset of Fig. 15). This feature implies the large β factor of the monopole-mode laser. We give its detailed estimation in the Section IV-C

Measured lasing frequencies from the samples with various lattice parameters are summarized as a function of the radius of the nearest neighbor holes in Fig. 16. These experimental data are plotted as dot symbols when the lattice constant

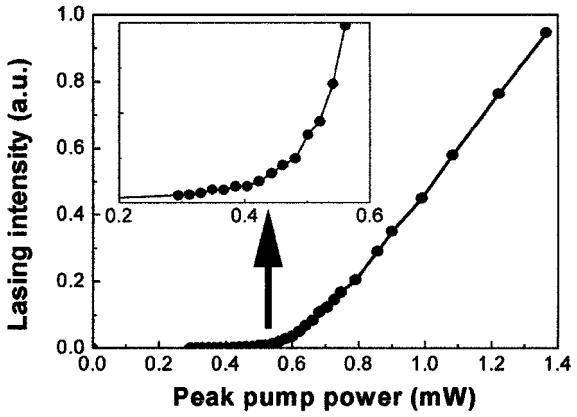

Fig. 15. Plot of the collected power at lasing wavelength versus the peak pump power (*L–L* curve) in the monopole-mode laser. Threshold pump power is less than 0.55 mW. Note that gradual turn on near the threshold (inset).

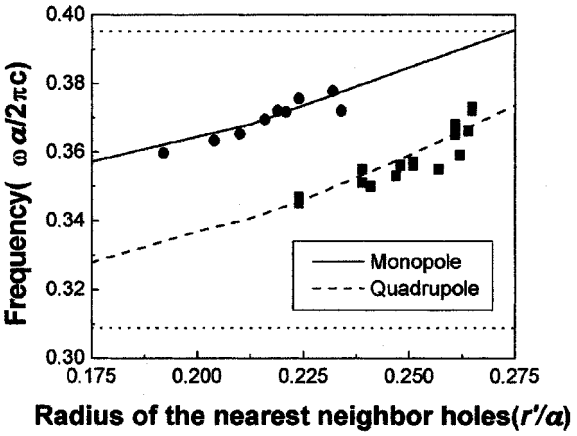

Fig. 16. Experimentally observed frequencies of lasing modes (dots) are compared with the calculated values (lines) when the radius of the nearest neighbor holes are varied. Both r and t are fixed to 0.35 a, which are the average values of the real samples. Circular dots agree well with the calculated frequencies of the monopole mode (solid line), and square dots follow the frequency dependence of quadrupole mode (dashed line). Two dotted lines represent band edge frequencies. At the region where monopole-mode lasing actions occurr, its Q factors have maximum values as seen in Fig. 13.

and regular hole size are fixed to their average values of $\sim$0.57 μm and $\sim$0.35 a, respectively. Circular dots indicate monopole-mode lasers and square dots the quadrupole-mode lasers. The dipole-mode lasers are not observed because of the modification of the structure. These two modes are compared with 3-D FDTD calculations performed from lattice parameters of actual fabricated samples. As can be seen in Fig. 16, good agreement is found between the experimental and the calculated results. If we observe this graph carefully, another interesting fact is found: the monopole-mode lasing actions do not occur at the center of the band gap, but rather slightly above it. This can be understood by considering the Q factor of the monopole mode of Fig. 13. That is, when the radius of the nearest neighbor holes around the defect is varied from 0.2 a to 0.225 a, the calculated Q factor is maximized, and simultaneous lasing actions are experimentally obtained.

From the *L–L* curves of lasing actions in the other modes, as well as the monopole mode, it is experimentally confirmed that each smallest threshold pump power is scarcely dependent on the kind of the mode. Various characteristics of several modes surely affect their lasing operations; e.g., the Q factor of the mode determines whether the lasing action is possible or not. And, by degeneracy or nondegeneracy, the spontaneous emission near the threshold is changed, as will be shown Section IV-C. Nevertheless, their threshold values are very similar each other. This fact tells us that the nonradiative recombination, common property in all modes, might be a limiting factor to determine the threshold. Specifically, surface recombination will be dominant because QWs of the PBG laser have a lot of air holes. In fact, the thresholds of our modified single-defect lasers are lower than that of a normal one [9]. It is because the modified structure, such as the reduced surface area by retreated location of the nearest holes, helps to reduce the surface recombination of carriers in the cavity region. Since the nonradiative processes can be suppressed in low temperature [15], the threshold can be lowered as well and unique characteristics of each mode will be clearly observed.

Next, we try to compare the experimentally measured mode shapes with the calculated ones of Fig. 4. Because the other modes often operating as multimode show mixed mode shapes, the monopole mode, always a single mode, is suitable for direct comparison with the calculation. In Fig. 17(a)–(c), the monopole-mode lasers are actually captured by IR vidicon camera with different imaging planes. Symmetric donut-shaped images are shown, and these are broader as the plane becomes farther away. The images agree well with the calculated results at different vertical positions as shown in Fig. 17(d)–(f). This consistency supports the fact that our laser is really of the monopole mode. Also, from this symmetric mode shape of the monopole mode, its polarization can be thought to have no definite direction. This is certainly confirmed by calculating the electric field direction of the monopole mode in Fig. 7(d). The monopole mode oscillates radially in the plane of the slab with respect to the center of the cavity. This genuine 2-D mode utilizing full 2-D PBG does not show any certain oscillating direction. In Fig. 18(a), a preferred polarization direction of the monopole-mode laser does not become experimentally clear by measuring lasing intensities with a polarizer in front of the spectrometer. The noncircular shape of the polarization data is attributed to the asymmetry of the fabricated hole patterns and polarization-dependent optical components. Similar discussion can be also applied to the quadrupole modes. In this sense, the polarization of the quadrupole mode shows a minimum along a certain direction [Fig. 18(b)], as we can guess from Fig. 7(b).

The calculated Q factors in Section IV-A can be compared with the experiments. By measuring the FWHM of a resonance peak at the transparent condition, the Q factors are experimentally determined. At the pumping power near the transparency, $\sim$0.48 mW, the below-threshold linewidth of the monopole mode is $\sim$0.8 nm, which is the resolution limit of our spectrometer. This value gives the lower bound of total Q factor of $\sim$2000, and agrees well with the calculated value $\sim$3700, in Fig. 13.

C. Spontaneous Emission Factor of the Monopole-Mode Laser

In 2-D PBG slab structures, some parts of the spontaneous emission are not guided by the slab, and are not coupled with cavity modes. Nevertheless, a large β factor near unity is theoretically possible because this leaky portion is relatively small

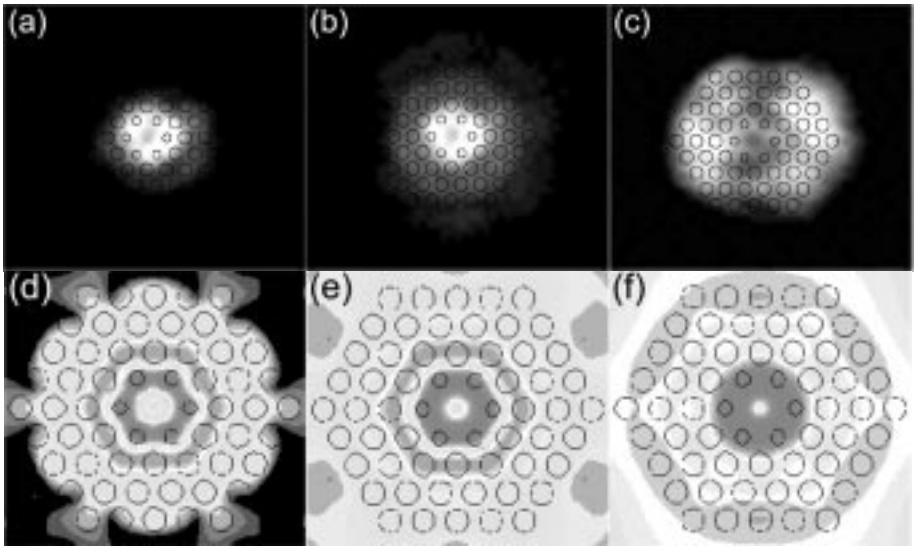

Fig. 17. (a)–(c) Experimental images of the monopole-mode lasers captured by IR-vidicon camera with different imaging planes. These agree well with the calculated images using the 3-D FDTD method at various vertical positions: (d) $z = \lambda$, (e) $z = 1.5\,\lambda$, and (f) $z = 3\,\lambda$. The thickness of the slab is $\sim\lambda/2$ and the origin is the center of the slab.

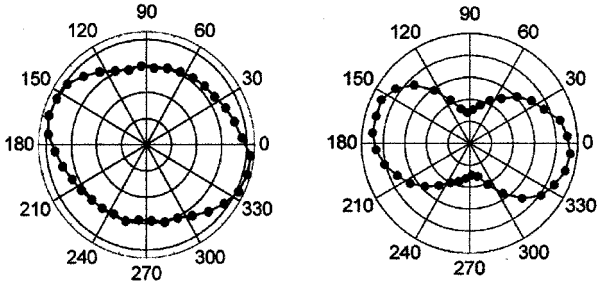

Fig. 18. Measured polarization directions of (a) the monopole-mode laser and (b) quadrupole-mode laser. In (a), no preferred direction is shown, as expected from the calculation. On the other hand, in (b), there exists a certain oscillating direction.

[21]. In this section, we estimate the β factor of the nondegenerate monopole-mode laser based on the theoretically obtained curves from the rate equation analysis. Since the theoretical curve characterizes the spectrally integrated mode power, the experimental output power should be also integrated for fair comparison. In the *L–L* curve of Fig. 15, the output lasing power was obtained from the peak intensity measured by the spectrometer with wide resolution covering the mode spectrum. Thus, this experimental curve can be reliably compared with the theoretical one [22].

Carrier density N and photon density P in the cavity are described by following conventional rate equations [3]:

$$\frac{dN}{dt} = \eta\frac{L_{in}}{\hbar\omega_p V_a} - \left(\frac{A_a}{V_a}v_s N + BN^2 + CN^3\right) - \Gamma G(N)P$$

$$\frac{dP}{dt} = \Gamma G(N)P - \frac{P}{\tau_p} + \beta BN^2$$

where η is the absorbed ratio in QWs, ω_p is the frequency of a 980-nm pumping laser, v_s is the nonradiative surface recombination velocity, B is the radiative recombination coefficient, C is the Auger nonradiative recombination coefficient, and Γ is the confinement factor. The photon lifetime τ_p is represented as follows: $\tau_p = \lambda Q/2\pi c$, where λ is the wavelength of the output laser and Q is the Q factor of the monopole mode. In these equations, A_a and V_a are the active surface area and the active region volume that are determined as the total sidewall area of air holes and the volume except air holes, respectively, in the pumped active region. Parameters except β are inserted in the above equations, and output power $L_{\text{out}} = \hbar\omega P V_a/\tau_p$ is plotted as a function of the pump power L_{in}. These parameters, summarized in Table I, are typical values for InGaAsP–InP multiple QWs (MQWs) at room temperature [23]. The logarithmic gain $G(N) = G_0(c/n_{eq})\ln(N/N_{tr})$ was assumed, where N_{tr} is the transparency carrier density and n_{eq} is the effective refractive index. As can be seen in Fig. 19(a), calculated curves (lines) are plotted with some different β values. Experimental data of the monopole mode obtained in Fig. 15 (circular dots) are together plotted. The experimental and theoretical curves are best agreed when $\beta = 0.0625$. For the comparison purpose,

TABLE I
PARAMETERS USED IN THE RATE EQUATIONS. THESE ARE TYPICAL VALUES FOR InGaAsP–InP MQWS AT ROOM TEMPERATURE

Parameters	Values
η	0.21
v_s	1×10^4 cm/s
B	1.6×10^{-10} cm^3/s
C	5.0×10^{-29} cm^6/s
Γ	0.2
λ	1.56 μm
n_{eq}	2.65
G_0	1500 cm^{-1}
N_{tr}	1.5×10^{18} cm^{-3}
Q	3500
A_a	2.20×10^{-8} cm^2
V_a	3.19×10^{-13} cm^3

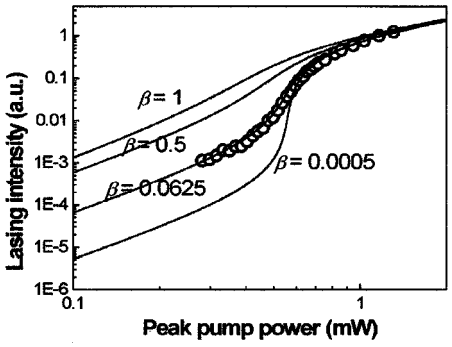

(a)

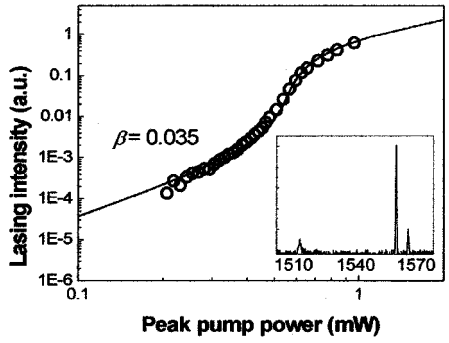

(b)

Fig. 19. (a) A log–log plot of the *L–L* curve of the monopole-mode laser. Dots show the experimental data of Fig. 15 and lines are theoretically obtained results by the rate equation analysis. When the β is $\sim$0.0625, experimental data is agreed well with the calculated results. (b) β factor of doubly degenerate modes is estimated under the same fitting condition. The inset indicates its typical above-threshold spectrum.

we also measured *L–L* curve of the doubly degenerate modes in Fig. 19(b) (dots). The inset of this figure represents its typical above-threshold spectrum. The *L–L* curve shows lower spontaneous emission below threshold than the monopole mode. Interestingly, the β factor of this mode is estimated to $\sim$0.035, about half of that of the monopole mode when all the parameters are the same as the previous fitting case. However, further study is necessary to confirm whether this decrease originates from the double degeneracy.

In the above analysis, a relatively large β value of the monopole mode $\sim$0.0625 is obtained as compared with those of other conventional semiconductor lasers $10^{-4}\sim10^{-5}$. However, this is smaller than the expected β value of $>$0.1. We can find some practical reasons for that. As shown in the inset of Fig. 14(b), additional nonlasing modes around the monopole mode disturb the single-mode coupling of the spontaneous emission even though they have low-Q factor and poor coupling efficiency with the gain medium. We can increase the β factor in two ways—by pulling apart these nonlasing modes from the PL spectrum or reducing the coupling efficiency further. From the structure of the elliptical-shaped nearest neighbor holes, this effect is expected, as mentioned in Section II. Alternatively, by using another active material having narrow bandwidth less than $\sim$50 nm, for example a single quantum-dot (QD) emitter, only the monopole mode can be allowed in the PL spectrum. In addition, if the lasing wavelength of the monopole mode exists at the peak of PL spectrum, the coupling efficiency will increase and a larger β factor be obtained [22], [23].

TABLE II
WE VARY THE DIAMETER OF THE PUMP SPOT (A_a, V_a), Q, AND η. IN THEIR REASONABLE RANGES, SEVERAL POSSIBLE β VALUES, FROM $\sim$0.035 TO $\sim$0.1025, ARE ESTIMATED

Diameter of pump spot (μm)	A_a ($\times 10^{-8}$ cm^2)	V_a ($\times 10^{-13}$ cm^3)	Q	η	β
3.8	1.99	2.94	2000	0.21	0.035
			3000	0.19	0.055
			5000	0.18	0.1
4.0	2.20	3.19	2000	0.23	0.035
			3500	0.21	0.0625
			4500	0.2	0.085
4.2	2.40	3.44	3000	0.23	0.06
			4000	0.22	0.08
			5500	0.21	0.1025

The above method to find the β value in the log–log plot of the *L–L* curve is commonly used for semiconductor devices [22]–[24]. In this process, however, the output curves obtained by the rate equations strongly depend on both β and other parameters listed in Table I. By some ambiguities of these parameters, the estimated β also has a room for variation. In our analyses, the reasonable ranges of A_a, V_a, Q, and η are tried. First, the active surface area A_a and the active volume V_a strongly affect the nonradiative surface recombination rate. The pump diameter larger than 4 μm is estimated from the diameter of PL on unpatterned region of the sample. In the PBG region, the pump spot could be slightly different from this volume since the carrier diffusion effect is changed by many holes. Next, the real Q factor can be larger than the experimental lower limit of 2000. And the upper bound of η is set to 0.225. Under these varying conditions, several possible β values are estimated and summarized in Table II. The β factor ranges from $\sim$0.035 to $\sim$0.1025.

In the *L–L* curve of Fig. 19(a), the below and above threshold regions are easily divided, although β values are reasonably large. This is attributed to the large surface recombination carrier losses generated at many air-hole interfaces of QWs. Note that even when β is unity, a linear *L–L* curve is not obtained if the nonradiative recombination is present as shown in Fig. 19(a). A true thresholdless laser will be realized only when this nonradiative surface recombination is practically suppressed. To this end, QDs can be used as an active material instead of QWs. By their low carrier diffusion, the surface recombination is reduced at low temperature. For a GaAs material system, the effective and reliable passivation process should be found [15].

V. CHARACTERISTICS OF RESONANT MODES IN EPOXY-BONDED OXIDE-CLADDING SLAB STRUCTURES

A. Calculation of Q Factors

The epoxy-bonded slab structure obtains both mechanical stability and good thermal conductivity by low index material below the slab, whose refractive index is 1.5. However, the vertical loss of this structure will be larger because the difference of refractive indices between the slab and bottom cladding regions decreases. The reduced Q factor disturbs the achievement of the lasing action. As discussed in Section IV, there exists a good correlation between the Q factor and the possibility of the lasing action. In this section, we try to calculate the Q factors

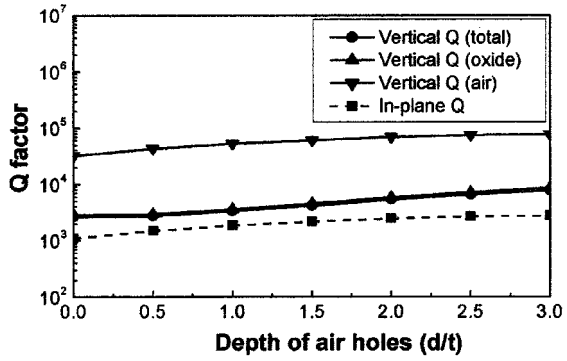

Fig. 20. Q factors of the monopole mode are calculated as a function of the depth of the air holes d. $r = 0.35\ a$, $r' = 0.25\ a$, and $t = 0.4\ a$ are also employed. Vertical losses are decomposed into two parts in this vertically asymmetric structure: losses fallen into the air and the bottom cladding (oxide) region.

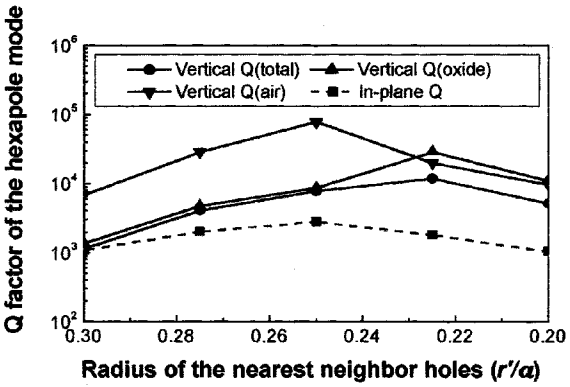

(a)

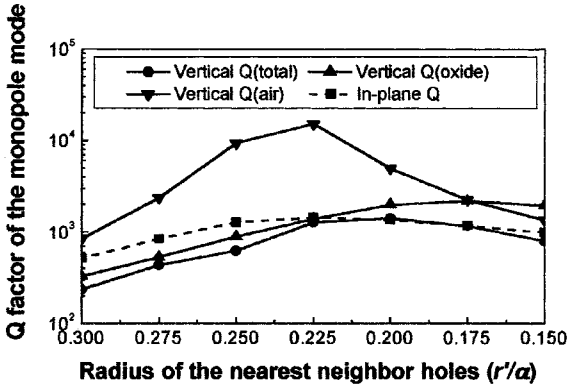

(b)

Fig. 21. In the structure with oxide bottom cladding, the calculated Q factors of (a) the hexapole and (b) the monopole mode as a function of the nearest neighbor holes. We set the parameters as follows: $r = 0.35\ a$, $t = 0.25\ a$, and $d = 5\ t$.

in the slab structure with oxide bottom cladding. Calculations are obtained in the same domain size as Section VI.

Vertical losses are separated by two parts in this asymmetric structure: energies propagating into the air and the bottom cladding (oxide) region, which are separately considered. It is easily shown that the losses by bottom oxide cladding are larger than those by the air region, and the total Q factor is limited by losses in oxide-cladding region. First, we check the effect of the depth of the air hole (d). In the defect structure of Fig. 2(a), regular and nearest neighbor hole sizes (r, r'), and slab thickness (t) are fixed to 0.35 a, 0.25 a, and 0.4 a, respectively. Fig. 20 shows vertical and in-plane Q factors of the monopole mode in this structure as a function of d. From the results of monotonically increased Q factors with the depth, it is known that the lasing action will be more advantageous in the case of deeper air holes. This is reasonable, considering the vertical confinement of photons becomes stronger when the air holes are deeper.

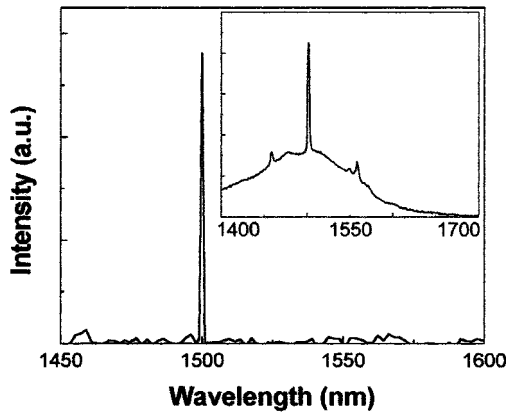

(a)

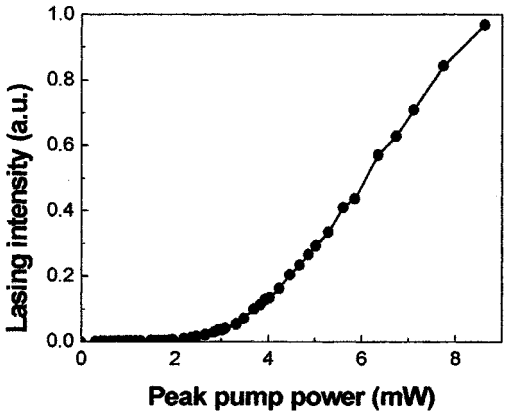

(b)

Fig. 22. (a) Typical above-threshold spectrum of a modified single-defect laser with oxide bottom cladding. Its below-threshold spectrum is shown in inset. Under pulse pumping condition of 10% duty cycle, lasing action is measured at 1500 nm wavelength. (b) An L–L curve of this laser. The threshold is ~2.5 mW.

We also calculate the Q factors of the hexapole and monopole modes as r' is varied. Other parameters are the same as in the above calculation, and d is chosen to be 2 a. Fig. 21(a) and (b) show these calculated results. As compared with the case of the free-standing structure, total vertical Q factors of both modes are much reduced. The maximum Q value of the hexapole mode is still large, ~12 000; on the other hand, that of the monopole mode is ~1400.

B. Experiments

With the same experimental setup as in Section IV-B, this modified single defect shows optically pulse-pumped lasing action from the epoxy-bonded samples. In this structure, owing to an improved thermal conductivity, the laser continues to operate even when the pulse width is increased up to ~150 ns in ~1 μs period (~15% duty cycle). Although the thermal conductivity of the bottom cladding region SiO_2 is excellent, the whole thermal conductivity of the structure is not good enough for CW operation because of the relatively poor thermal conductivity of the epoxy.

This is the first demonstration of the single-defect PBG slab laser with a low index material, such as SiO_2. Fig. 22(a) shows

the lasing spectrum above and below (inset) threshold , measured with pulses of a ∼10% duty cycle. In order to identify the lasing modes, more samples with various lattice parameters should be prepared and analyzed. A *L–L* curve of this laser is shown in Fig. 22(b). The threshold pump power is ∼2.5 mW. With further optimization, this type of single-defect PBG laser could operate not only with lower threshold, but also under CW pumping conditions.

VI. Conclusion

We introduced and analyzed various resonant modes found in a modified single-defect slab structure. Characteristics of each mode are theoretically obtained under the several conditions of structures, such as different shapes of the nearest neighbor holes (circular and elliptical), kinds of bottom cladding, slab thickness, and so on. Various interesting laser modes are experimentally observed from the free-standing slab structure. The observed lasers report high-Q factors and low-threshold values. The monopole-mode laser, especially, attracts our interest because of its nondegeneracy and good coupling with the gain medium. The monopole-mode laser shows a large β value between ∼0.035 and ∼0.1025, which is estimated from theoretically obtained curves by rate equations. Although these lasers operate only with short pulses, structures with oxide bottom cladding have a better chance with broader pulses due to their improved thermal conductivities. We also claim the first successful demonstration of a single-defect PBG laser made of oxide cladding. From advantages of this structure, both CW lasing operation and electrical pumping are expected.

Characteristics of the monopole mode, such as high-Q factors, low thresholds, and large β factors, indicate a possibility for a near-thresholdless laser. If we can reduce the nonradiative surface recombination, this goal will be fulfilled in the near future. As another candidate, we consider the hexapole mode with very high-Q factor. The hexapole mode will be specifically advantageous in the structure having a low index material as bottom cladding because its Q factor is still large while those of the other modes are heavily reduced in this structure. Although the hexapole mode is located close to the quadrupole modes, is disadvantageous to single-mode operation, and has poor coupling with the gain medium, these problems will be solved by optimizing the structure.

Acknowledgment

The authors would like to thank Dr. J. H. Shin of Electronics and Telecommunications Research Institute for helpful discussions.

References

[1] H. Yokoyama, "Physics and device applications of optical microcavities," *Science*, vol. 256, pp. 66–70, 1992.

[2] G. Björk and Y. Yamamoto, "Analysis of semiconductor microcavity lasers using rate equations," *IEEE J. Quantum Electron.*, vol. 27, pp. 2386–2396, 1991.

[3] T. Baba, "Photonic crystals and microdisk cavities based on GaInAsP–InP system," *IEEE J. Select. Topics Quantum Electron.*, vol. 3, pp. 808–830, 1997.

[4] T. F. Krauss and R. M. De La Rue, "Photonic crystals in the optical regime—Past, present and future," *Prog. Quantum Electron.*, vol. 23, pp. 51–96, 1999.

[5] H. G. Park, J. K. Hwang, J. Huh, H. Y. Ryu, Y. H. Lee, and J. S. Kim, "Nondegenerate monopole-mode two-dimensional photonic band gap laser," *Appl. Phys. Lett.*, vol. 79, pp. 3032–3034, 2001.

[6] P. R. Villeneuve, S. Fan, S. G. Johnson, and J. D. Joannopoulos, "Three-dimensional photon confinement in photonic crystals of low-dimensional periodicity," *Proc. Inst. Elect. Eng.–Optoelectron.*, vol. 145, pp. 384–390, 1998.

[7] O. Painter, J. Vučković, and A. Scherer, "Defect modes of a two-dimensional photonic crystal in an optically thin dielectric slab," *J. Opt. Soc. Amer. B*, vol. 16, pp. 275–285, 1999.

[8] O. Painter, R. K. Lee, A. Scherer, A. Yariv, J. D. O'Brien, P. D. Dapkus, and I. Kim, "Two-dimensional photonic band-gap defect mode laser," *Science*, vol. 284, pp. 1819–1821, 1999.

[9] O. J. Painter, A. Husain, A. Sherer, J. D. O'Brien, I. Kim, and P. D. Dapkus, "Room temperature photonic crystal defect lasers at near-infrared wavelengths in InGaAsP," *J. Lightwave Technol.*, vol. 17, pp. 2082–2088, 1999.

[10] J. K. Hwang, H. Y. Ryu, D. S. Song, I. Y. Han, H. W. Song, H. K. Park, Y. H. Lee, and D. H. Jang, "Room-temperature triangular-lattice two-dimensional photonic band gap lasers operating at 1.54 μm," *Appl. Phys. Lett.*, vol. 76, pp. 2982–2984, 2000.

[11] J. K. Hwang, H. Y. Ryu, D. S. Song, I. Y. Han, H. K. Park, D. H. Jang, and Y. H. Lee, "Continuous room-temperature operation of optically pumped two-dimensional photonic crystal lasers at 1.6 μm," *IEEE Photon. Technol. Lett.*, vol. 12, pp. 1295–1297, 2000.

[12] H. Y. Ryu, S. H. Kim, H. G. Park, J. K. Hwang, Y. H. Lee, and J. S. Kim, "Square-lattice photonic band-gap single-cell laser operating in the lowest-order whispering gallery mode," *Appl. Phys. Lett.*, vol. 80, pp. 3883–3885, 2002.

[13] O. Painter and K. Srinivasan, "Polarization properties of dipolelike defect modes in photonic crystal nanocavities," *Opt. Lett.*, vol. 27, pp. 339–341, 2002.

[14] A. Taflove, *Computational Electrodynamics—The Finite-Difference Time-Domain Method*. Boston, MA: Artech House, 1995.

[15] L. A. Coldren and S. W. Corzine, *Diode Lasers and Photonic Integrated Circuits*. New York: Wiley, 1995.

[16] J. D. Joannopoulos, R. D. Meade, and J. N. Winn, *Photonic Crystals*. Princeton, NJ: Princeton Univ., 1995.

[17] M. Boroditsky, T. F. Krauss, R. Coccioli, R. Vrijen, R. Bhat, and E. Yablonovitch, "Light extraction from optically pumped light-emitting diode by thin-slab photonic crystals," *Appl. Phys. Lett.*, vol. 75, pp. 1036–1038, 1999.

[18] M. Boroditsky, R. Vrijen, T. F. Krauss, R. Coccioli, R. Bhat, and E. Yablonovitch, "Spontaneous emission extraction and Purcell enhancement from thin-film 2-D photonic crystals," *J. Lightwave Technol.*, vol. 17, pp. 2096–2112, 1999.

[19] T. Baba, N. Fukaya, and J. Yonekura, "Observation of light propagation in photonic crystal optical waveguides with bends," *Electron. Lett.*, vol. 35, pp. 654–655, 1999.

[20] J. Huh, J. K. Hwang, H. Y. Ryu, and Y. H. Lee, "Nondegenerate monopole mode of single defect two-dimensional triangular photonic band gap cavity," J. Appl. Phys., to be published.

[21] J. Vučković, O. Painter, X. Yong, A. Yariv, and A. Scherer, "Finite-difference time-domain calculation of the spontaneous emission coupling factor in optical microcavities," *IEEE J. Quantum Electron.*, vol. 35, pp. 1168–1175, 1999.

[22] M. Fujita, R. Ushigome, and T. Baba, "Large spontaneous emission factor of 0.1 in a microdisk injection laser," *IEEE Photon. Technol. Lett.*, vol. 13, pp. 403–405, 2001.

[23] M. Fujita, A. Sakai, and T. Baba, "Ultrasmall and ultralow threshold GaInAsP–InP microdisk injection lasers: Design, fabrication, lasing characteristics, and spontaneous emission factor," *IEEE J. Select. Topics Quantum Electron.*, vol. 5, pp. 673–681, 1999.

[24] W. D. Zhou, J. Sabarinathan, P. Bhattacharya, B. Kochman, E. W. Berg, P. C. Yu, and S. W. Pang, "Characteristics of a photonic bandgap single defect microcavity electroluminescent device," *IEEE J. Quantum Electron.*, vol. 37, pp. 1153–1160, 2001.

Hong-Gyu Park was born in Seoul City, Korea, in 1976. He received the B.S. and M.S. degrees in 1998 and 2000, respectively, from the Department of Physics, Korea Advanced Institute of Science and Technology (KAIST), Taejon, where he is currently working toward the Ph.D. degree, studying the design, fabrication, and characterization of photonic crystal light-emitting structures.

Jeong-Ki Hwang received the B.S., M.S., and Ph.D. degrees from the Department of Physics, Korea Advanced Institute of Science and Technology (KAIST), Taejon, in 1994, 1996, and 2000, respectively. During his Ph.D. work, he studied spontaneous and stimulated emission control in photonic bandgap cavities.

He is currently with the Networking Solution Division, Agilent Technologies, San Jose, CA.

Jonn Huh was born in Seoul City, Korea, in 1960. He received the B.S. degree from the Department of Applied Physics, Inha University, in 1984, and the M.S. and Ph.D. degrees from the Department of Physics, Korea Advanced Institute of Science and Technology (KAIST), Taejon, in 1987 and 2002, respectively. During his Ph.D. work, he studied resonant modes of two-dimensional slab triangular photonic crystal cavities.

He is currently with the Agency for Defense Development (ADD), Taejon, Korea.

Han-Youl Ryu was born in Taegu City, Korea, in 1974. He received the B.S., M.S., and Ph.D. degrees from the Department of Physics, Korea Advanced Institute of Science and Technology (KAIST), Taejon, in 1996, 1998, and 2002, respectively. During his Ph.D. work, he studied photonic crystal slab light-emitting structures.

Se-Heon Kim was born in Seoul City, Korea, in 1978. He received the B.S. and M.S. degrees from the Department of Physics, Korea Advanced Institute of Science and Technology (KAIST), Taejon, in 2000 and 2002, respectively. During his M.S. work, he studied photonic crystal lasers.

Jeong-Soo Kim, photograph and biography not available at the time of publication.

Yong-Hee Lee received the M.S. degree in applied physics from Korea Advanced Institute of Science and Technology (KAIST), Taejon, and the Ph.D. degree in optical sciences from the University of Arizona, Tucson.

He is currently a Professor in the Department of Physics, KAIST, where he has been since 1991. He was previously with AT&T Bell Laboratories, where he demonstrated the first proton-implanted VCSELs in 1990 and holds the original patent on this industrial VCSEL. His research interests lies in thresholdless photonic bandgap lasers and nano-photonic integrated optical circuits, as well as VCSELs. He has coauthored more than 90 international journal papers and patents related to VCSELs and photonic bandgap structures.